

Contents lists available at ScienceDirect

Nuclear Instruments and Methods in Physics Research A

journal homepage: www.elsevier.com/locate/nima



Design and construction of the fast photon detection system for **COMPASS RICH-1**

- P. Abbon ^k, M. Alexeev ^{a,1}, H. Angerer ⁱ, R. Birsa ^o, P. Bordalo ^{g,2}, F. Bradamante ⁿ, A. Bressan ⁿ, M. Chiosso ¹, P. Ciliberti ⁿ, M. Colantoni ^m, T. Dafni ^k, S. Dalla Torre ^{o,*}, E. Delagnes ^k, O. Denisov ^m, H. Deschamps ^k, V. Diaz ^o, N. Dibiase ¹, V. Duic ⁿ, W. Eyrich ^d, A. Ferrero ¹, M. Finger ^j, M. Finger Jr. ^j, H. Fischer ^e,

- S. Gerassimovⁱ, M. Giorgiⁿ, B. Gobbo^o, R. Hagemann^e, D. von Harrach^h, F.H. Heinsius^e, R. Joosten^b,
- B. Ketzerⁱ, V.N. Kolosov^{c,3}, K. Königsmann^e, I. Konorovⁱ, D. Kramer^{c,f}, F. Kunne^k, A. Lehmann^d, S. Levoratoⁿ, A. Maggiora^m, A. Magnon^k, A. Mannⁱ, A. Martinⁿ, G. Menon^o, A. Mutter^e, O. Nähle^b,
- F. Nerling^e, D. Neyret^k, D. Panzieri^a, S. Paulⁱ, G. Pesaroⁿ, C. Pizzolotto^d, J. Polak^{f,o}, P. Rebourgeard^k,
- F. Robinet ^k, E. Rocco ^l, P. Schiavon ⁿ, C. Schill ^e, P. Schoenmeier ^d, W. Schröder ^d, L. Silva ^g, M. Slunecka ^j, F. Sozzi ⁿ, L. Steiger ^j, M. Sulc ^f, M. Svec ^f, S. Takekawa ⁿ, F. Tessarotto ^o, A. Teufel ^d, H. Wollny ^e
- ^a INFN, Sezione di Torino and University of East Piemonte, Alessandria, Italy
- ^b Universität Bonn, Helmholtz-Institut für Strahlen- und Kernphysik, Bonn, Germany
- ^c CERN, European Organization for Nuclear Research, Geneva, Switzerland
- ^d Universität Erlangen-Nürnberg, Physikalisches Institut, Erlangen, Germany
- e Universität Freiburg, Physikalisches Institut, Freiburg, Germany
- ^f Technical University of Liberec, Liberec, Czech Republic
- ^g LIP, Lisbon, Portugal
- ^h Universität Mainz, Institut für Kernphysik, Mainz, Germany
- ⁱ Technische Universität München, Physik Department, Garching, Germany
- ^j Charles University, Prague, Czech Republic and JINR, Dubna, Russia
- k CEA Saclay, DSM/DAPNIA, Gif-sur-Yvette, France
- ¹ INFN, Sezione di Torino and University of Torino, Torino, Italy
- ^m INFN, Sezione di Torino, Torino, Italy
- ⁿ INFN, Sezione di Trieste and University of Trieste, Trieste, Italy
- ° INFN, Sezione di Trieste, Trieste, Italy

ARTICLE INFO

Article history: Received 28 July 2009 Received in revised form 5 February 2010 Accepted 9 February 2010 Available online 1 March 2010

Keywords: COMPASS Multi-anode photo-multiplier Particle identification Ouartz lens telescope

ABSTRACT

New photon detectors, based on the use of multi-anode photo-multiplier tubes coupled to individual lens telescopes and read out with a dedicated read-out electronics system, equip the central region of the Cherenkov imaging counter RICH-1 of the COMPASS experiment at CERN SPS. They are characterised by high photon yield, fast response and high rate capability and are successfully in operation since the 2006 COMPASS data taking. The photon detection system fully matches the expected performance.

The design and construction of the photon detectors are described in detail.

© 2010 Elsevier B.V. All rights reserved.

1. Introduction

The COMPASS experiment [1,2] at the CERN SPS is dedicated to hadron physics with a two-fold programme; the nucleon spin structure is studied using the CERN SPS polarised muon beam and solid state deuterium or hydrogen targets, longitudinally or transversely polarised; hadron spectroscopy is explored using

Corresponding author.

E-mail address: silvia.dallatorre@ts.infn.it (S. Dalla Torre).

¹ On leave from JINR, Dubna, Russia.

² Also at IST, Universidade Técnica de Lisboa, Lisbon, Portugal.

³ On leave from IHEP, Protvino, Russia.

pion and proton beams. All features of the experimental setup are described in Ref. [3]. Here we recall that the whole COMPASS research programme requires high luminosity, namely working at high beam and trigger rates. Another overall request is to perform hadron identification in difficult environments, characterised by large rates of uncorrelated background events due to either the large dispersed halo accompanying the muon beam, extended over square metres, or the secondary particles generated by the hadron beam interactions in the apparatus material.

In COMPASS, hadron identification is performed with RICH-1 [4], a large size Ring Imaging CHerenkov counter in operation at COMPASS since 2002. During the years 2001–2004, photon detection with RICH-1 has been performed by Multi-Wire Proportional Chambers (MWPC) equipped with CsI photocathodes [5]. Some characteristic features of these photon detectors and of its associate front-end read-out electronics (Section 2) limit the RICH-1 performance in the COMPASS environment, reducing the efficiency in particular for particles scattered at small angles and introducing some dead-time in the experiment data acquisition. To overcome these limitations, the photon detection system of the RICH-1 counter has been upgraded.

In the peripheral region, which amounts to 75% of the active surface, the photon detectors are unchanged since the level of uncorrelated background is not very large. The read-out, however, is now based on a new system [6] with the APV chip [7] with negligible dead-time and improved time resolution. The central photon detection area (25% of the active surface) is both highly populated by uncorrelated background images with photon rates up to 1 MHz per channel, corresponding to an $8 \times 8 \text{ mm}^2$ pad, and it includes the large majority of the high momentum hadron images, as these particles are scattered at small angles. The uncorrelated background signals can be rejected by finer time resolution, while good Cherenkov angle resolution is the handle for effective identification of high momentum hadrons. These requisites, together with high rate capability, dictate the main design criteria of the new photon detection system. This system is now in operation since the 2006 data taking.

The present article is dedicated to the new photon detection system of the central region of COMPASS RICH-1. The performance of RICH-1 before the upgrade is recalled in Section 2. The new photon detection system is outlined in Section 3. Sections 4–7 present the design, description and construction of the various system components. In Section 8 the performance of the new photon detectors is given. Section 9 is dedicated to conclusions.

2. COMPASS RICH-1 performance before the counter upgrade

COMPASS RICH-1 [4] is a gaseous RICH with large transverse size to match the acceptance of the first stage of the COMPASS spectrometer [3]. Its main components are the radiator gas, C_4F_{10} , included in a gas tight vessel, pressure controlled and purified with a dedicated gas system [8], the UV mirror system [9] and the photon detectors, namely MWPCs with CsI photo-cathode with photon conversion capability in the VUV domain, below 200 nm. The active surface is $5.3 \, \mathrm{m}^2$. The MWPC gas is separated from the radiator vessel one by fused silica windows, which are not transparent below $\sim 165 \, \mathrm{nm}$. The images collected in the photon detectors are pseudo-circular and we will refer to them as rings. The basic parameters characterising the detector performances are the mean number of detected photons: 14 per particle with

 $\beta \rightarrow$ 1, the single photon resolution on the measured Cherenkov angle, σ_{ph} : 1.2 mrad for particle with $\beta \rightarrow$ 1, the global resolution on the measured Cherenkov angle, σ_{ring} : 0.6 mrad for particle with $\beta \rightarrow$ 1, a PID efficiency larger than 95% for Cherenkov angles larger than 30 mrad and a $2-\sigma$ $\pi-K$ separation at 43 GeV/c [4,10].

In spite of these remarkable figures, there are some performance limitations. The presence of the CsI photo-converter imposes to operate the MWPCs at a rather low gain (below 5×10^4) to guarantee their electrical stability. The first stage of the electronics read-out system is based on a modified version of the front-end Gassiplex-chip [11], amplifying and shaping the signal with a rather long integration time (0.6 μ s) to compensate for the reduced gain. The typical noise figure obtained is 1100 electrons equivalent. The low gain, the integration time and an effective threshold at 3–3.5 times the noise level result in a detection efficiency for single photoelectrons, which ranges around 70%.

The Gassiplex integration time acts as a detector memory: each event image collected by the photon detectors includes the information of uncorrelated background events. Due to the nature of the background, the related rings cluster in the central region of the photon detectors. The high level background limits both the RICH-1 efficiency and the resolution.

The efficiency drops for very forward scattered particles, due to the combination of two effects, namely the high level background images present in the central photon detector region and due to photon losses: part of the Cherenkov photons generated by the forward scattered particles are lost due to the central dead zones of RICH-1, present to screen the photon detectors from the photons generated by the non-interacting beam.

The background also limits the RICH-1 resolution in the measured Cherenkov angle. This effect is evident considering the measured resolution values of the Cherenkov angle. σ_{ph} and σ_{ring} do not scale according to the square root of the number of photons: the actual value of σ_{ring} is almost a factor of two worse, due to the presence of the high level background.

3. The new photon detection system of the central region of COMPASS RICH-1

The new photon detectors of COMPASS RICH-1 [12] are based on the use of Multi-Anode Photo-Multiplier Tubes (MAPMTs) as active elements. MAPMTs, intrinsically fast and with sub-ns time resolution, are read out via a digital system based on highly sensitive amplifier-discriminators and high resolution Time to Digital Converters (TDCs) [13]. The choice of a digital system matches well the MAPMT characteristics: the spread amplitude spectrum provided by this photon detector (Section 4) would limit the effectiveness of the photon counting via amplitude measurement. The MAPMTs are coupled to individual telescopes of fused silica lenses to enlarge the effective detection area. A compact setup with negligible dead zones and able to ensure both light and gas tightness has been obtained with a careful design, construction and assembly of the mechanical components of the setup.

MAPMTs coupled to lens telescopes have already been successfully employed for single photon detection in the HeraB RICH counter [14,15]. They have been proposed as one of the options for photon detection in LHCb RICHes [16]. Our approach is characterised by some novel features:

• the photon wavelength domain is extended to the UV range, thanks to the use of MAPMTs with UV extended window, that allows to convert photons down to 200 nm wavelength, and to the choice of telescopes formed by fused silica lenses;

⁴ The ideal circular image is distorted, mainly because it is formed on the planar detector surface, which approximates the spherical focal surface of the mirror wall.

- the demagnification parameter of the telescopes coupled to each MAPMT is large; this makes it possible to get a surface ratio between the entrance window of each telescope and the photo-cathode larger than 7; this feature, coupled to an accurate arrangement of the MAPMT and lens mechanical supports, allows both to save on the number of MAPMTs required, and to obtain a dead zone fraction of ~2% only;
- the read-out is performed by a system providing a high sensitive front-end stage, resulting in a high detection efficiency for the single photoelectron, sub-ns time resolution to minimise the background due to uncorrelated events and to fully exploit the MAPMT time resolution, and high rate capabilities, as required by the high luminosity of the COMPASS experiment.

3.1. Number of detected photons and resolution considerations

The main motivations for the upgrade are to obtain high rate capability and to decrease the background down to a negligible level. Concerning the resolution in the measured Cherenkov angle, the goal is to recover the figure spoilt by the background presence, namely to get a r.m.s. of ~ 0.3 mrad (Section 2).

Comparing photon detection with MWPCs equipped with CsI photo-cathodes (i), to the photon detection performed with MAPMTs (ii), two major differences have to be taken into account. The converted Cherenkov photons have wavelengths spanning different ranges, which results in a different effective refractive index of the radiator gas (Fig. 1) and in a different chromatic dispersion. Folding the refractive index with the Cherenkov spectrum and the detector quantum efficiency (for MWPCs with CsI photocathode [5]; for MAPMTs, Fig. 1 and Section 4), the resulting dispersion of the refractive index has a r.m.s. of 30×10^{-6} for (i), and 46×10^{-6} for (ii). Concerning the number of detected photons, taking into account the Cherenkov spectrum, the quantum efficiency and the photoelectron detection efficiency, the number of detected photons per active surface unit is about 4 times larger for (ii) then for (i). This opens the possibility of detecting a larger number of photons per ring using the MAPMTs.

A larger number of detected photons can compensate for the resolution worsening caused by an enlarged effective pixel size. The MAPMTs photo-cathode size and pixel size are fixed, but the use of an optical system in front of the MAPMT can enlarge the

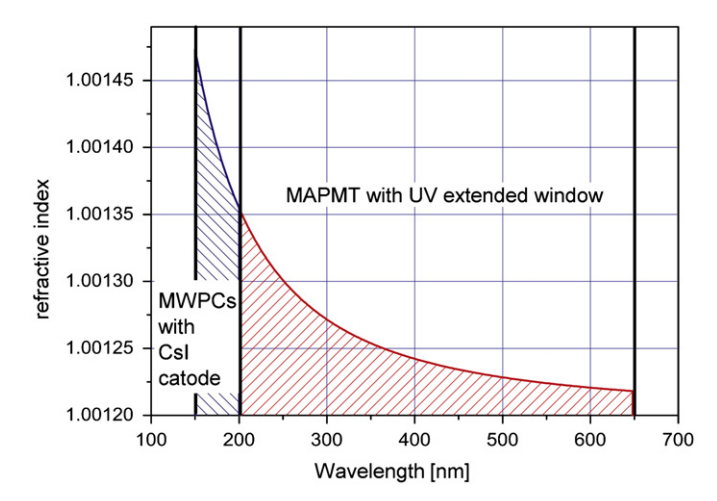


Fig. 1. Measured C_4F_{10} refractive index versus light wavelength at STP; data from Ref. [17]. The wavelength ranges of effective quantum efficiency for the MWPCs with CsI photo-cathodes and for MAPMTs with extended UV glass windows (Section 4) are indicated.

effective size of the cathode surface and, correspondingly, of the pixel. This approach has several advantages:

- it makes it possible to recover for the intrinsic dead zone between adjacent MAPMTs, due to the external MAPMT dimension:
- enlarging even more the distance between adjacent MAPMTs, it is possible to reduce the number of MAPMTs needed, making the project economically affordable;
- a large number of photons per ring is detected. The increased chromatic dispersion is more than compensated by averaging over a larger number of detected photons. The larger number of detected photons is an important handle to increase the RICH-1 efficiency for those images, for which the number of photons is reduced, namely at very small scattering angles, due to the dead zones at the RICH centre, and for particles with momenta near to the threshold of the Cherenkov emission.

The effective pixel size cannot be enlarged excessively. In fact, if the pixel size becomes too large, the probability of having more photoelectrons in the same pixel becomes important. Using a digital read-out system, this corresponds to an effective reduction in the number of detected photons. Another reason to limit the effective pixel size are the distortions that large image demagnification introduces. The selected MAPMTs (Section 4) have a photocathode area of $18 \times 18 \text{ mm}^2$, segmented so to form a 4×4 matrix, while the transverse size of the PMT is $26 \times 26 \,\mathrm{mm}^2$. On the base of the considerations presented above and taking into account the MAPMT characteristics, an effective pixel size of about $12 \times 12 \text{ mm}^2$ has been chosen. Assuming no dead areas between the effective active surface of adjacent MAPMTs this results in a MAPMT pitch of ~ 5 cm, corresponding to the need of 576 MAPMTs to instrument the central region of COMPASS RICH-1.

4. The multi-anode photomultipliers

The MAPMT type R7600-03-M16 by Hamamatsu, 5 with 16 anode channels, bi-alkali photo-cathode and UV extended glass window, has been chosen to detect single photons at high rates. Fig. 2 shows the quantum efficiency of one of the MAPMT used, provided by Hamamatsu measuring the cathode photocurrent. These MAPMTs are characterised by large gain (at least 10^6 at $800\,\mathrm{V}$), fast transit time ($\sim 10\,\mathrm{ns}$) and fast anode signal rise time ($< 1\,\mathrm{ns}$). They have been equipped with a custom voltage divider circuit, reproducing the standard configuration proposed by Hamamatsu [18]. The MAPMT response to single photons has been characterised; these studies are described elsewhere [13]. In the following we recall the basic features. The MAPMT pixel labelling used, with numbers from 1 to 16, is according to Ref. [18] (Fig. 3).

Part of the photoelectrons entering the multiplication chain do not experience the whole 12-dynode stages and thus the response to single photoelectrons results in a 2-peak amplitude spectrum with a typical ratio between the two mean amplitudes of a factor between 3 and 4. This feature has already been observed [19]. Good single photoelectron detection efficiency requires detecting the signals included in both peaks: with our front-end electronics 95% of the signals are detected, applying a threshold setting that allows to reject both the noise peak, which is completely suppressed, and to reduce the rate of the cross-talk between channels in the same MAPMT to < 0.1% [13].

⁵ Hamamatsu Photonics K.K., http://www.hamamatsu.com.

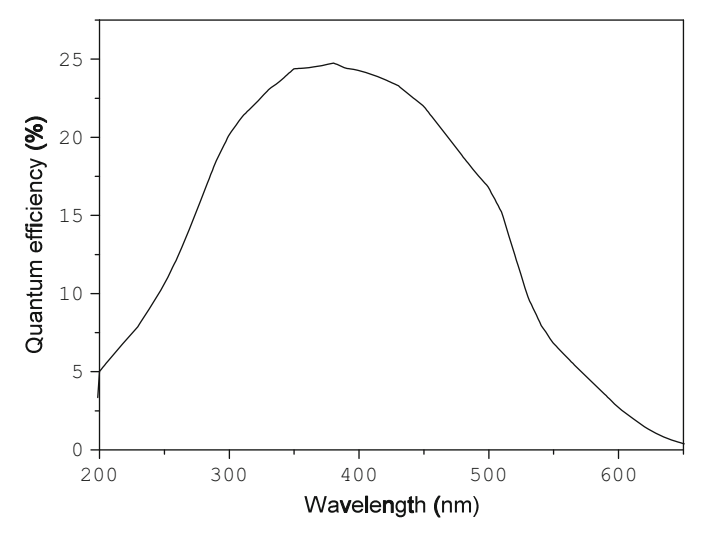


Fig. 2. Effective quantum efficiency determined by measuring the cathode photocurrent for a MAPMT used in the project.

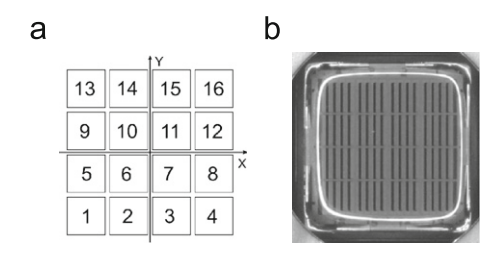


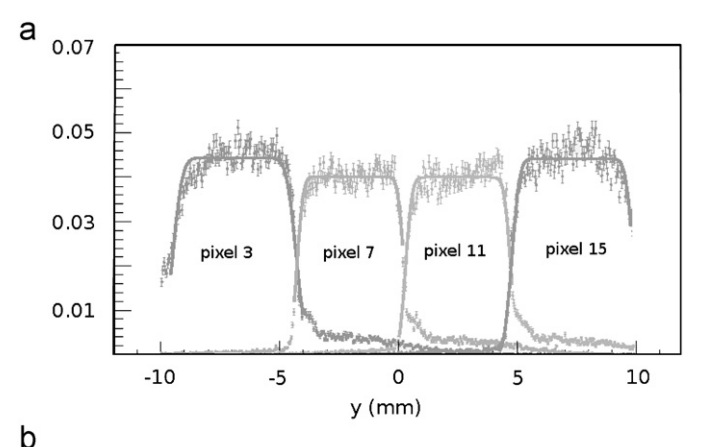
Fig. 3. (a) MAPMT pixel labels, following [18], view from photo-cathode side. (b) Picture of the photo-cathode of a MAPMT; the orientation in (a) and (b) is the same.

The MAPMT can sustain single photoelectron rates higher than 5 MHz per channel without exhibiting gain reduction. The time resolution measured with our read-out system (Section 5) is 320 ps r.m.s. for the central peak of the time spectrum; in addition, there is a tail of later signals related to photons impinging on the photo-cathode close to the border between two neighbouring channels.

The pixel size given in Ref. [18] is $4.2 \times 4.2 \, \text{mm}^2$ for the central pixels and slightly more for the external ones. The effective pixel size has been measured by a position scan measurement performed with a light source with a diameter of about 0.1 mm r.m.s. (Fig. 4) [20]. The pixel width is obtained with a best fit procedure describing the pixel response with a function obtained adding a box function and two gaussian functions with central value corresponding to the box edges. The fitted box width is assumed as the pixel size. The measured pixel sizes are reported in Table 1. The plots in Fig. 4 also indicate that the external pixels exhibit a higher signal yield.

4.1. MAPMTs operation in low magnetic field

The MAPMT type R7600-03-M16 is sensitive to magnetic fields: in presence of a non-zero field a reduced response is observed, in principle due to the combination of two possible effects: (i) more photoelectrons do not enter the multiplication chain (about 70% are accepted when there is no magnetic field) and (ii) the gain is reduced. For the detection of single photons, effect (i) results in a net decrease of the detection efficiency, while effect (ii) can be tolerated, provided that the gain reduction is limited. In the COMPASS application, MAPMTs have to operate in



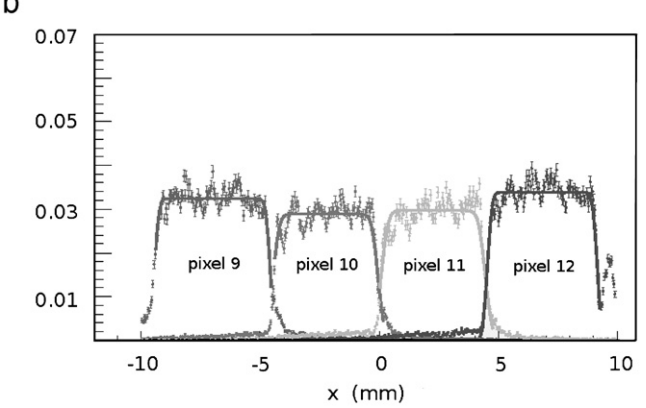


Fig. 4. Measurement of the effective MAPMT pixel size performed by scanning the MAPMT anode response with a light source with a dimension of 0.1 mm r.m.s. The scan step is 0.05 mm. The scan has been performed both by row (b) and by column (a).

Table 1 Measured pixel size.

Scanning by row		Scanning by colu	umn
Pixel label Pixel width (mm)		Pixel label	Pixel width (mm)
9	4.9 4.4	3 7	5.2 4.5
11	4.4	11	4.4
12	4.6	15	5.1

a region with magnetic field up to 20 mT, with its main component parallel to the MAPMT axis. The field is due to the fringing field of the open H-shaped spectrometer magnet placed a few metres upstream of the RICH-1 counter.

We have characterised the single photoelectron response of the MAPMT in moderate magnetic fields parallel to the MAPMT axis [20,21]. The magnetic field has been generated with a Helmholtz coil⁶ with an internal diameter of 26 cm, a total length of 24 cm, providing a constant magnetic field in a 20 cm long region. The magnetic field has been measured with a Hall probe sensor type GM05 gaussmeter by Hirst Magnetic Instruments Ltd.⁷ The MAPMTs have been read out using the digital electronics system described in Section 5. The characterisation studies have been performed illuminating the MAPMT photo-cathodes with

⁶ Courtesy of Prof. K. Kuroda.

⁷ Hirst Magnetic Instruments Ltd, Tesla House, Tregoniggie Falmouth, Cornwall TR11 4SN, UK.

light pulses attenuated in order to provide single photoelectron conditions. The light pulses were provided by an LED powered with reversed bias, so to be able to obtain short pulses (typical pulse length: \sim 20 ns). Threshold curves, as those shown in Fig. 5, are taken in different field conditions: the plateau value, normalised to the value obtained with no magnetic field, provides the relative efficiency variation. Repeated measurements with no magnetic field indicate that the overall stability of the results obtained with this method is at a level better than 3%. It has been seen that the pixels in a row exhibit a very similar response variation in magnetic fields: in Fig. 6 the response of the pixels of the same column are averaged, the response averaged over the whole set of 16 pixels of a MAPMT is also shown. The plot in Fig. 6 (a) clearly indicates a drastic decrease of the occupancy averaged over the whole set of 16 pixels outside the magnetic field range of \pm 2 mT; in Fig. 6 (b) a zoom of the central portion of the same plot is shown: also for the pixels of one of the two central columns (pixels 2, 6, 10 and 14) the occupancy is constant in the range -2to +2 mT, while for the external column (pixels 1, 5, 9 and 13) there is an occupancy increase between $-2 \, \text{mT}$ and zero field and a corresponding decrease between zero field and +2 mT. A similar behaviour is seen for the other two columns, provided that the

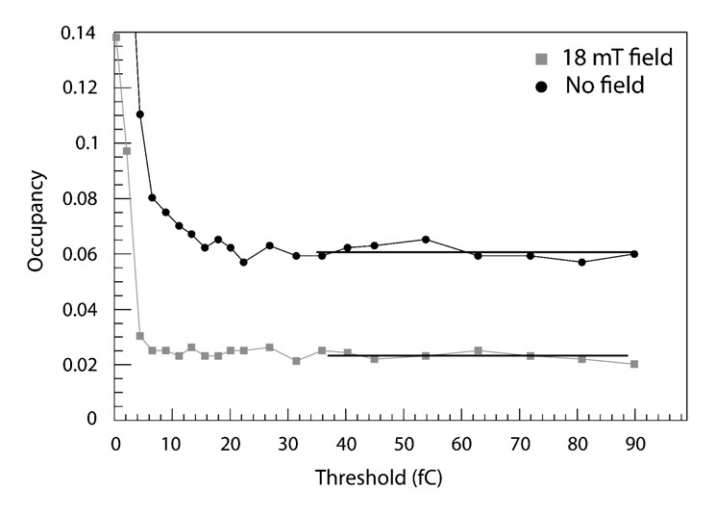


Fig. 5. Threshold curves for one of the 16 anodes of a MAPMT in different magnetic field conditions: no field and 18 mT. The channel occupancy is plotted versus threshold setting. The illumination conditions are constant during the measurement

magnetic field orientation is reversed. In the range -2 to+2 mT the effect of the magnetic field is to slightly modify the acceptance of the MAPMT multiplication chains, in particular in the external pixel columns, without a substantial variation of the global efficiency. Outside the region ± 2 mT, there is a net reduction of the acceptance of the multiplication chain resulting in an important reduction of the single photoelectron detection efficiency. It is interesting to notice that, for those photoelectrons being multiplied, the gain is not reduced for external fields as high as 20 mT: in fact the plateau of the threshold curves starts at unchanged threshold values (Fig. 5).

Our measurement of the effect of the magnetic field is in agreement with the effect measured by Hamamatsu for the MAPMTs R7600, 16 anodes, in spite of the different measuring technique: Hamamatsu results are obtained by illuminating the photo-cathode and measuring the anode current. This agreement is another confirmation that the predominant mechanism is (i).

In our application we can tolerate a small acceptance shift, caused by the presence of the magnetic field, but not an efficiency decrease: the MAPMT magnetic shielding must ensure to expose the MAPMT to a magnetic field with field strength below 2 mT. Individual soft iron boxes have been designed and built to surround the MAPMTs equipped with the voltage dividers (Fig. 7); in the front side, the box is protruded and supports the concentrator lens of the lens telescope (Section 6), in the rear side, small openings are provided for the front-end boards, which are directly inserted in connectors present on the voltage divider PCB. The field inside the box has been measured for different values of the external field (Fig. 8). For an external field of 22 mT, the internal field in the region where the MAPMT is located does not exceed 1 mT.

4.2. The MAPMT quality assessment

The MAPMT specifications are given in Table 2. A quality control protocol [22] has been established to asses the quality of the MAPMTs needed for the upgraded photon detection system and to guarantee that they are operated at the optimum working point. The sample consists of 642 MAPMTs in total, including the spare units, corresponding to more than 10 k anode channels. For this purpose, a fully automated test setup was designed and assembled.

The quality control setup allows to test all the 16 channels of a MAPMT in parallel. A LED pulsing system illuminates

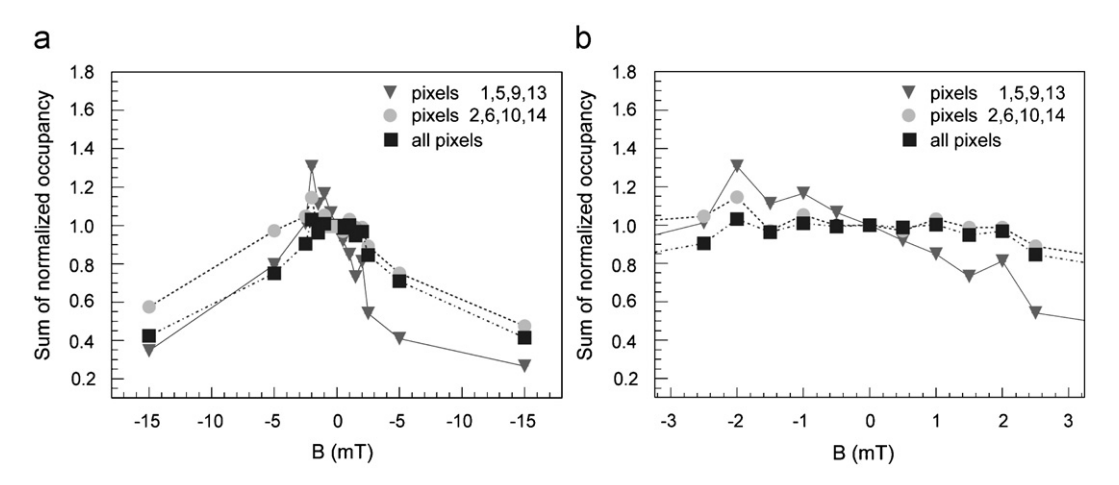


Fig. 6. Sum of the occupancy of the MAPMT pixels, normalised to zero field, versus magnetic field: a column of external pixels, namely pixels 1, 5, 9, and 13; a column of internal pixels, namely pixels 2,6, 10, 14; all 16 pixels. The magnetic field is parallel to the MAPMT axis and oriented from the photo-cathode towards the anodes. The plot in (b) is a zoom of the central portion of the plot in (a); the error bars are negligible in this scale.

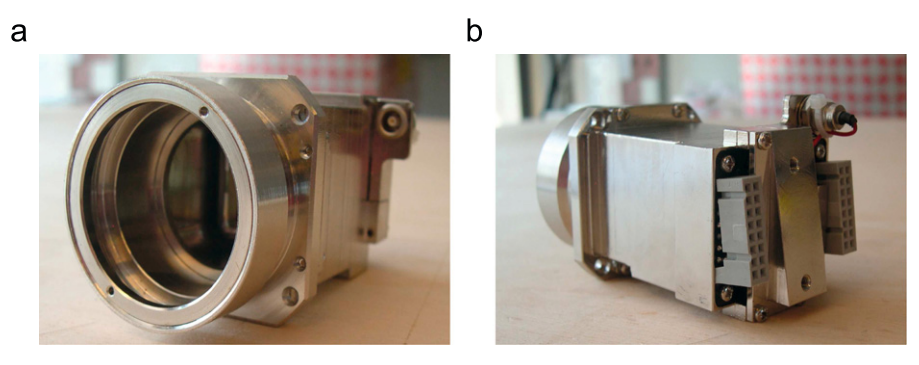


Fig. 7. MAPMT individual magnetic shielding by soft iron; (a) front view; (b) rear view.

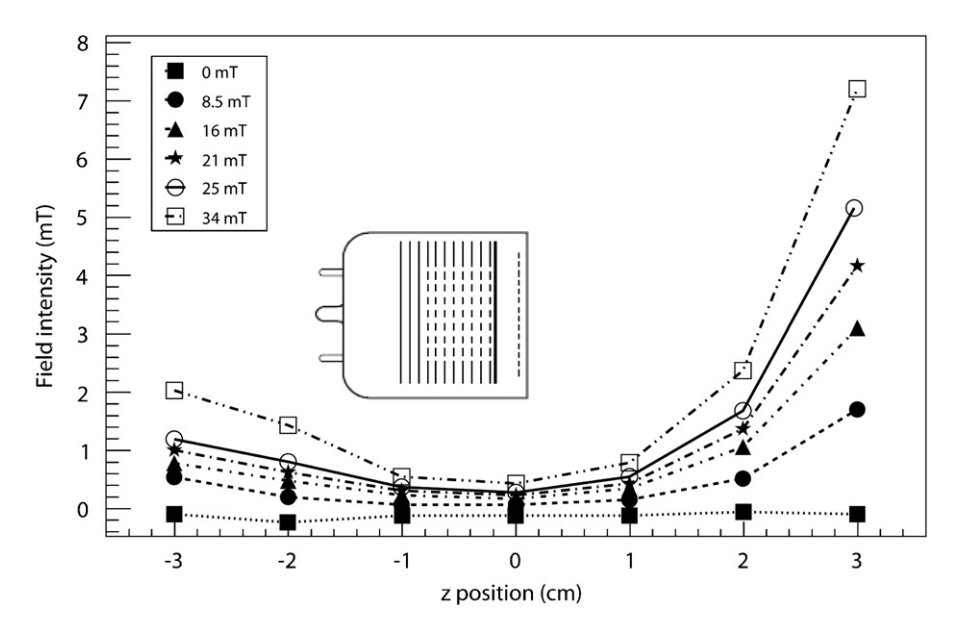


Fig. 8. Magnetic field inside the shielding-box versus the position along the axis of the shielding-box for different values of the external field. The MAPMT position inside the box is indicated.

Table 2Parameters characterising the MAPMTs used for the COMPASS RICH-1 Upgrade.

Parameter	Standard value
Photo-cathode surface Multiplicative chain Gain Anode DC per channel Total DC Anode signal rise time Signal transit time Uniformity between anodes QE at 420 nm QE at 250 nm	18.1 × 18.1 mm ² (minimum) 12 dynodes 3.5 × 10 ⁶ (typical) (*) > 1 × 10 ⁶ at 800 V 0.8 nA (typical), 60 nA (maximum) 0.83 ns (typical) 10.9 ns (typical) 1:2.5 (typical) (*) 1:3 (maximum) > 20% (*) > 5%

The standard values are from Ref. [18]; some parameters are required for our application (*).

homogeneously the photo-cathode of the MAPMT and concurrently generates a trigger signal as gate for the charge-to-digital converter (QDC). To study single photon response, attenuation filters are placed directly in front of the LEDs. The measurement protocol of each MAPMT includes: the visual inspection of the cathode surface, the recording of QDC spectra at five different high voltage values (from 850 to 970 V in steps of 30 V) for two different wavelength values each (360 and 480 nm), recording of

oscilloscope images, and the analysis of the amplitude spectra of all the channels at maximum high voltage level. Right before and after data recording, the dark current of all 16 channels is measured. In general, the dark current registered at the end of the measurement protocol lasting two hours, is an order of magnitude less than specified. During each test, no significant room temperature changes occurred. The measurement procedure is immediately followed by data analysis, determining anode uniformity, relative quantum efficiency and gain.

Fig. 9 shows one of the typical single photon QDC distributions obtained. Beside the QDC pedestal, two main components are visible. They correspond to the signals of the photoelectrons subjected to the full 12 step amplification chain, and those for which an amplification stage was missed. Mean value and standard deviation of each contributing peak are determined by a two-gaussian fit. The uniformity of each MAPMT and the gain behaviour of each individual channel are extracted from these parameters (Fig. 10).

The quality of the MAPMT sample examined is very good. The resulting rejection rate is pretty low: one MAPMT is dead, one MAPMT exhibits a few degree misalignment of the metallic dynode set, 20 MAPMTs are rejected because too high dark current has been measured for one or two anodes. Quantum efficiency, gain values and homogeneity are within specifications for the whole sample. The uniformity behaviour turned out to be

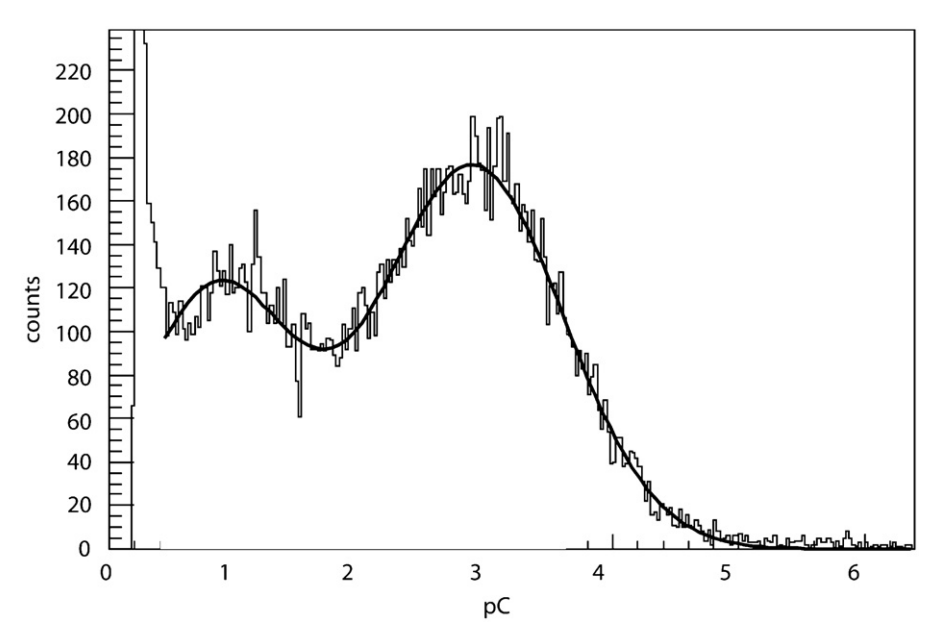


Fig. 9. Typical single photoelectron response measured at 970 V using 360 nm photons. The solid line is obtained by a two-gaussing best fit procedure.

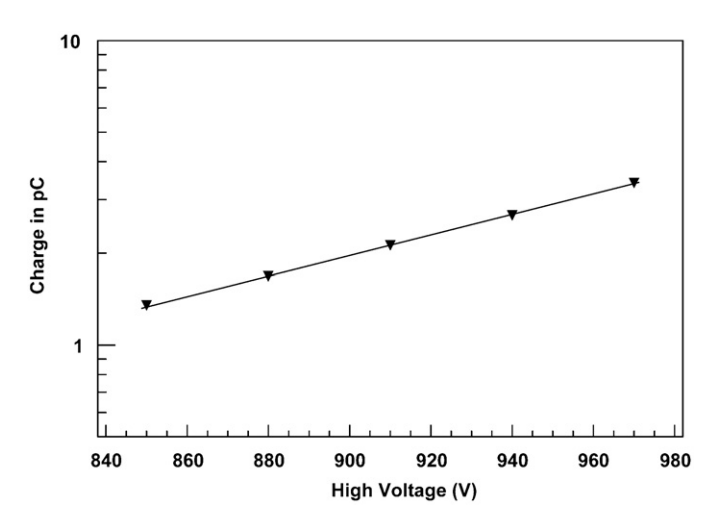


Fig. 10. Output charge of a MAPMT channel for single photoelectron. The curve is the exponential fitted function. The output charge is doubled increasing the voltage by 50 V.

largely better than specifications, with amplitude variations of only 20–30%.

The ideal high voltage setting for each MAPMT is the minimum value which guarantees at least 95% efficiency for all the MAPMT channels coupled to the front-end readout chain, based on the MAD4 discriminator boards [13]: this corresponds to a minimum output charge of 1.7 pC (gain $\sim 10^7$). The HV setting is deduced from an exponential best fit of the measured gain data. Fig. 11 shows the calculated high voltages for a sub sample of 556 MAPMTs. These values are gaussian distributed around 890 V with a standard deviation of $\sim 40\,\text{V}$. The central value corresponds pretty well to the typical value given by Hamamatsu ($\sim 910\,\text{V}$ for an amplification of $\sim 10^7$).

5. The read-out electronics system

The digital read-out system is based on the MAD4 preamplifier-discriminator [23] and the high resolution dead-time free F1 TDC [24]. The read-out system design, construction and performances are described in detail in Ref. [13]. Here we summarise its main features.

All read-out electronics are mounted in a very compact setup as close as possible to the photo-multipliers. The read-out system is free from cable connections to minimise the electrical noise, and to obtain a very robust setup. The system includes the following components: the front-end MAD4 boards, the service Roof boards, the DREISAM read-out boards, the HOT-CMC receiver board, the CATCH boards, the electronics cooling system and the mechanical structure to support the components of the read-out, which also guarantees good electrical contact between the different boards. The front-end MAD4 boards, housing the MAD4 preamplifier-discriminators, are plugged directly to the MAPMT voltage divider board where also the anode signals are available. The Roof boards provide services to the MAD4 boards: power, the DAC for threshold setting, and input/output data transfer from and to the digital board. The DREISAM read-out boards host eight F1 TDC chips each, for the read-out of the RICH-1 detector. The data transfer between DREISAM boards and CATCH boards is done via two optical links, to avoid ground loops. At the CATCH board, the optical connections are provided by the HOT-CMC mezzanine board. In CATCH boards, the data are formatted and sent via optical S-LINK links to the PCs of the COMPASS data acquisition [3].

The front-end analog stage, based on the MAD4 amplifier-discriminator chip, is capable to sustain an event rate up to 1 MHz per channel. The DREISAM board has been tested at trigger rates up to 100 kHz. For this digital board, a time jitter of < 35 ps r.m.s. for every individual channel versus a reference TDC was measured.

6. The lens telescope

To concentrate the light to the MAPMT photo-cathode preserving the position information a two-lens telescope was designed.

6.1. Orientation and acceptance of the lens telescope

The requirements concerning orientation and angular acceptance of the lens telescope have been determined with Monte

Carlo studies and are partially different according to the physics process considered. As reference, the most challenging physics channel for the RICH-1 performance within the COMPASS research programme, has been used: the detection of the decay channels $D^0 \rightarrow K^-\pi^+$ and $\overline{D}^0 \rightarrow K^+\pi^-$. A sample of these events has been generated using AROMA [25] and traced along the COMPASS spectrometer with GEANT 3.21 [26], making use of COMGEANT [3], the dedicated interface to GEANT developed in order to simulate the performance of the COMPASS spectrometer. The horizontal and vertical projections of the angle of the Cherenkov photons produced in RICH-1 by the charged hadrons from $D^0 - (\overline{D}^0)$ decay are shown in Fig. 12. These plots concern one of the four quadrants of the central region of RICH-1 photon detection area; the information about the other quadrants can be obtained applying the appropriate reflections. The quadrant surface is divided into 16 sectors, in order to analyse the angle evolution versus the position on the detector. The mean values of these distributions are plotted in Fig. 13, where the error bars represent the $\pm 1\sigma$ width of the same distributions. For comparison, also mean values and widths from analogous distributions produced using a different generator, Lepto [27], to simulate the hadron distribution from minimum bias Deep Inelastic Scattering (DIS) events, are shown. The orientation of the optical telescope axis and its angular acceptance, defined as the angular range for which the photon acceptance is larger than 50%, for the final telescope design (Section 6.2) are also plotted. The distributions present more critical features in the horizontal projection, as the mean values exhibit large variations and the distributions are wider. For this projection, a further check of the choice concerning the telescope orientation is obtained evaluating the fraction of rings, for which more than 50% of the generated Cherenkov photons are not accepted, versus the telescope horizontal inclination for various ranges in particle polar angle, for the hadrons from $D^0 - (\overline{D}^0 -)$ decay; the results are plotted in Fig. 14, assuming the telescope opening angle of the final design.

The optimal telescope orientation was fixed at 5.5° for the horizontal projection and 23.5° for the vertical one.

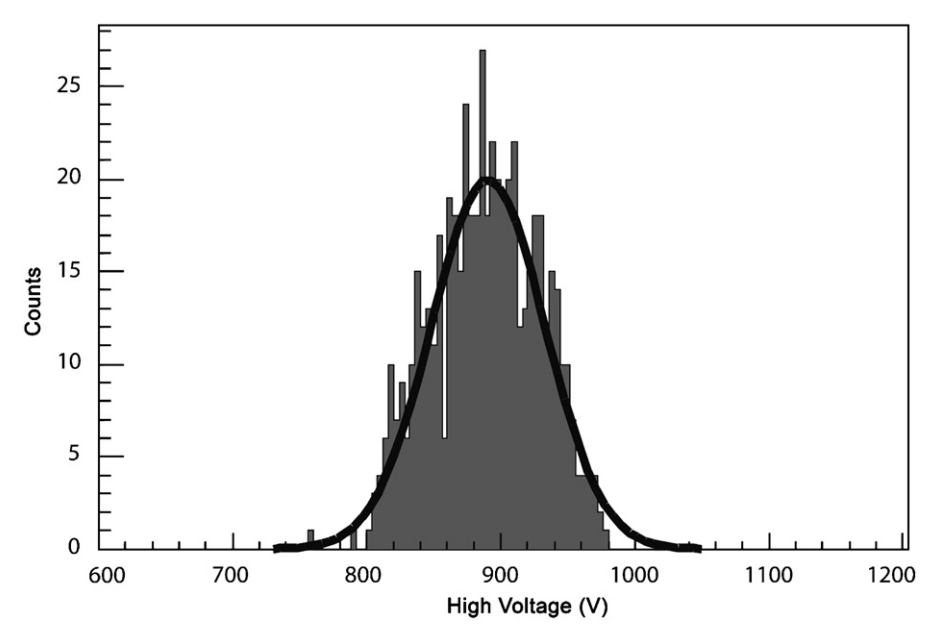


Fig. 11. Distribution of the high voltage value needed to get a minimum output charge of 1.7 pC for a sample of 556 MAPMTs.

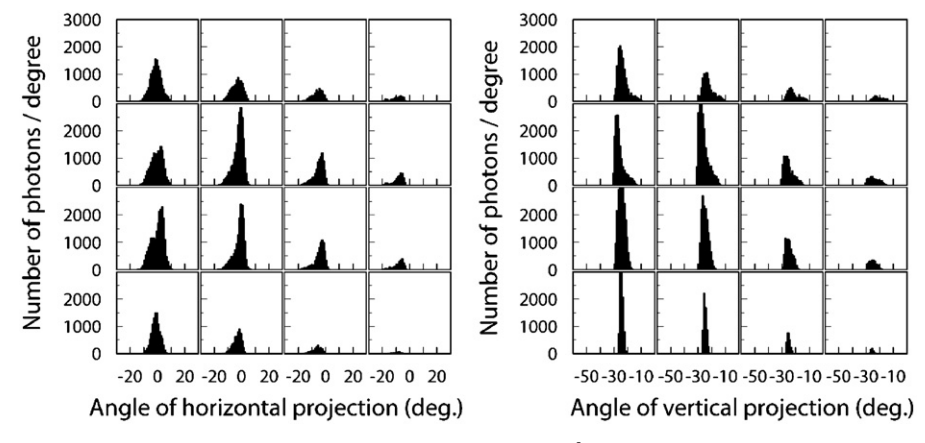


Fig. 12. Projections of the angle of the Cherenkov photons produced by the hadrons from $D^0 - (\overline{D}^0)$ decay from a sample of simulated events (simulation details in the text). The projection planes are orthogonal one respect to the other and respect to the detector holder plane, which is tilted by 8.6 degrees respect to the vertical plane; the first projection plane is parallel to the horizontal axis, the second one parallel to the vertical axis. The distributions are relative to the photons impinging on one of the four quadrants of the central region of RICH-1, dividing the quadrant surface in 16 sectors.

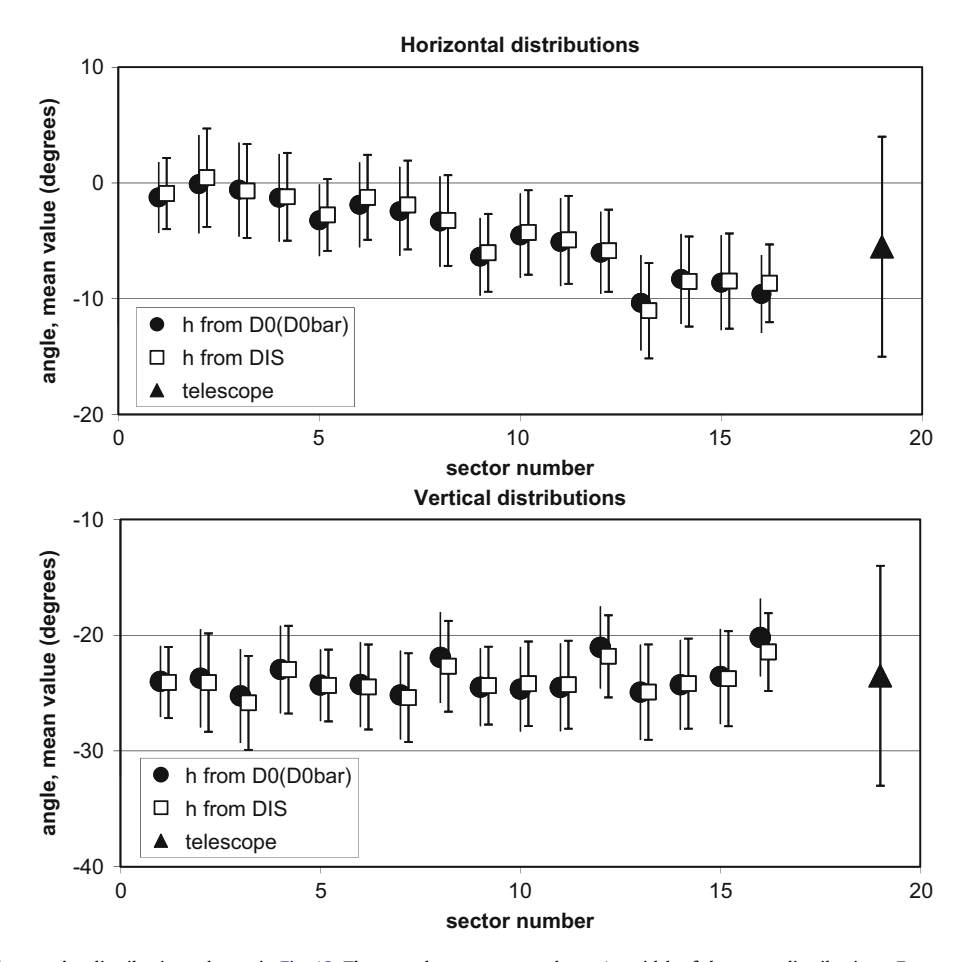
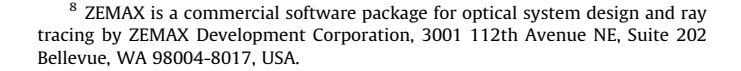


Fig. 13. Mean values of the angular distributions shown in Fig. 12. The error bars represent the $\pm 1\sigma$ width of the same distributions. For comparison, the central values and width of a hadron sample of simulated minimum bias DIS events are also plotted (simulation details in the text). The telescope orientation and opening angle of the final design is also shown.

6.2. The design of the lens telescope

The design of the lens telescope [28] has been performed using ZEMAX.⁸ The design of an optical system to collect Cherenkov light requires an unusual approach: the standard ray tracing, which starts from the object to be observed, cannot be applied due to the specific properties of the Cherenkov radiation. A light beam simulating the Cherenkov light is obtained with a parallel beam deviated by an ideal paraxial lens with focal length equal to its distance from the telescope field lens and placed at large distance: a distance of 100 m was used. The aperture of this lens matches the angular spectrum of the Cherenkov photons impinging on the telescope. The four wavelengths used have been weighted with the Cherenkov spectrum and the effective quantum efficiency of the MAPMTs: they are 220, 300, 400 and 600 nm and the maximum weight is at 300 nm.

In the optimisation procedure of the various designs of the telescope architecture, a merit function is needed. In the merit function used, the image performances in the different field positions are considered with the same weight: in our application we aim, as much as possible, at a similar image quality in all the positions.



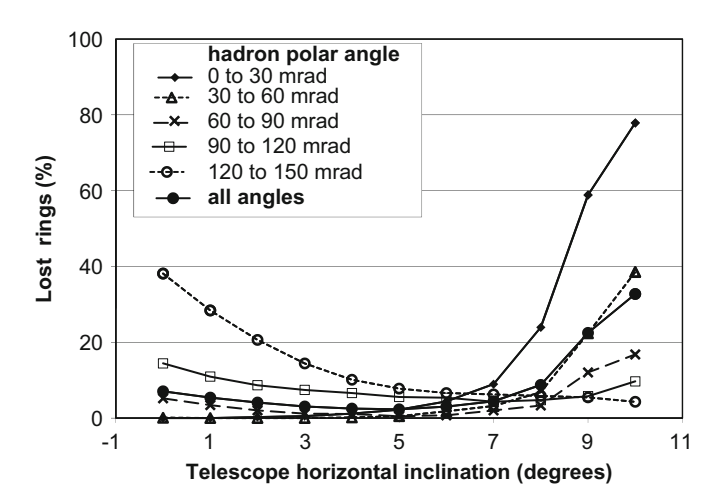


Fig. 14. Fraction of rings, for which more than 50% of the generated Cherenkov photons are not accepted, versus the telescope horizontal inclination for different particle polar angle ranges, for the hadrons from $D^0 - (\overline{D}^0 -)$ decay; the telescope opening angle of the final design, namely $\pm 9.5^\circ$, is assumed.

The requirements concerning the effective pixel size and MAPMT pitch coming from the overall project design (Section 3.1) are taken into account. Two constraints come from the existing COMPASS spectrometer set-up. The total telescope length cannot exceed 15 cm, due to the reduced space available

upstream of RICH-1 in the COMPASS spectrometer. The MAPMT has to be oriented at an angle with respect to the telescope entrance axis, a feature needed for compatibility with the existing MWPCs that remain as peripheral photon detectors: the telescope has to be a non-axial system.

To match the requirements, the telescope has to include a field lens followed by a concentrator, for a total of 4 lens surfaces; this basic scheme is derived from the one used for HeraB RICH [15], with a major modification: the field lens has to include a wedge element to get the needed non-axial telescope architecture. As a

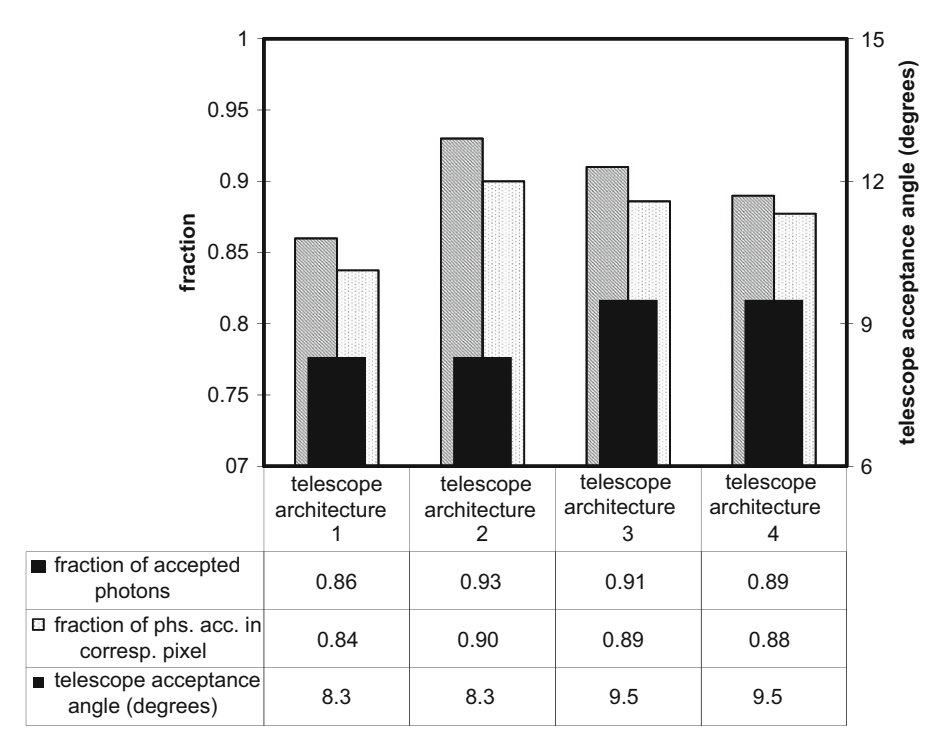


Fig. 15. Performance figures for the four different telescope architectures considered, evaluated with a simulation (details are in the text).

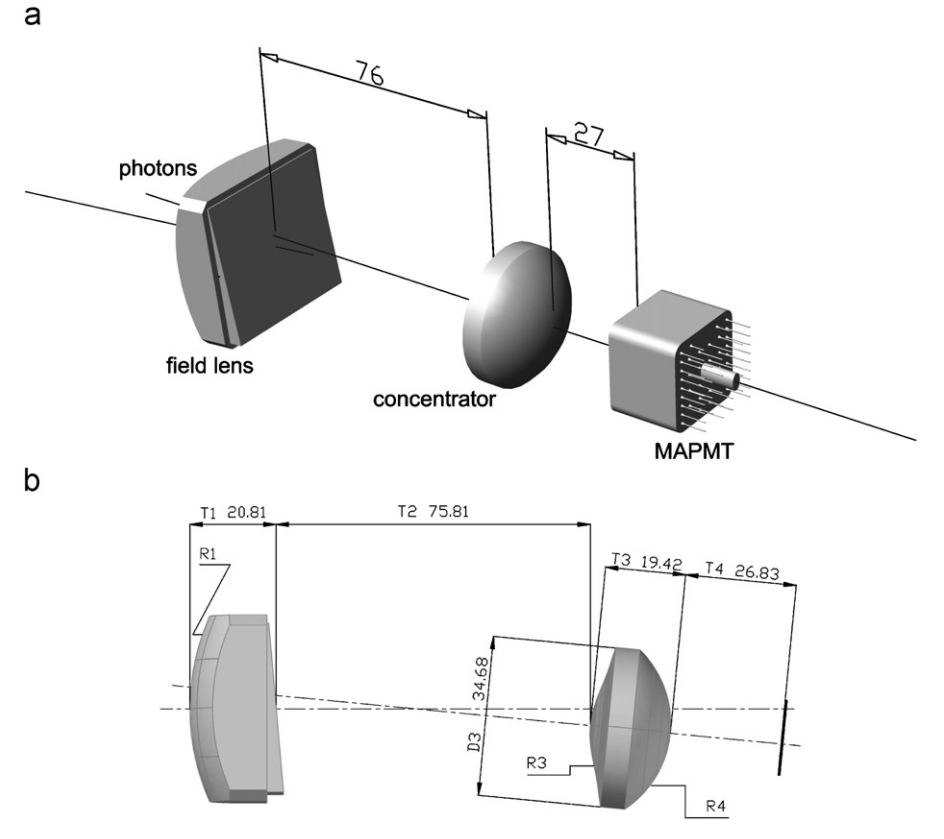


Fig. 16. The final design of the telescope; (a) artistic view; (b) side view (parameters are given in mm and quoted in Table 3).

consequence, we have chosen to have the second face of the field lens planar. Different telescope architectures have been derived from this basic scheme, and, for each architecture, an optimisation was performed. The architectures considered are:

- Architecture 1 is obtained assuming spherical shapes for three lens surfaces and an angular acceptance of ±8.3°.
- In architecture 2, there are two spherical and one aspherical lens surface; the angular acceptance is ±8.3°.
- \bullet Architecture 3 requires one spherical and two aspherical surfaces; the angular acceptance is $\pm\,9.5^\circ$.
- Architecture 4 is obtained with one field lens formed with a spherical surface and one concentrator with a spherical and one aspherical surface; the angular acceptance is $\pm 9.5^{\circ}$.

The optimal architecture has been selected according to the following criteria:

- maximise the photon acceptance;
- minimise the image distortions; and
- take into account the production and cost aspects.

The comparison of the optimised telescope designs for the different architectures is performed using the Monte Carlo options available in ZEMAX. In a plane surface orthogonal to the field lens axis and tangent to the lens spherical surface, a square area of $48 \times 48 \, \mathrm{mm^2}$, centred on the axis itself, is defined, indicated in the following as entrance window. This area is

Table 3 Parameters of the telescope.

Parameter	Value	
R_1 (mm) R_3 (mm) R_4 (mm) $\alpha \times 10^5$ (mm ⁻³) T_1 (mm) T_2 (mm) T_3 (mm)	54.937 20.696 -24.964 - 6.13884 20.813 75.805 19.420 26.835	
T_4 (mm) D_3 (mm)	34.68	

 R_1 , R_3 and R_4 are the radius of curvature of the optical surfaces, α is the aspherical 4th order coefficient of the third surface, T_1 , T_2 , T_3 and T_4 are the distances between the surfaces, D is the diameter of the concentrator; the role of the various parameters is illustrated in Fig. 16.

divided into a matrix of 4×4 identical square sectors, indicated in the following as pseudo-pads. A correspondence is established between the pseudo-pads and the 16 MAPMT pixels, taking into account that the telescope has an inverting optics. A light beam is generated according to the parameter distribution described above and traced through the telescope. Two ratios are evaluated using the simulated data. The fraction of accepted photons is the ratio between the number of photons crossing the entrance window and hitting the MAPMT photo-cathode surface and the total number of photons entering the entrance window. For each pixel, the fraction of photon accepted in the corresponding pixel is given by the ratio between the number of photons entering the a MAPMT pixel and the number of photons entering the corresponding pseudo-pad. The comparison is summarised in Fig. 15, where, for each architecture, the telescope acceptance angle and the values of the ratios described above, averaged over the 16 pseudo-pads, are plotted. Architectures 2, 3 and 4 have comparable figures for the ratios; architecture 3 and 4 provide larger angular acceptance, architecture 4 is definitely easier and cheaper to be produced, requiring a single aspherical surface. Architecture 4 has been adopted; it is shown in detail in Fig. 16. The equation describing the aspherical surface is

$$z = \frac{\rho^2 / R}{1 + \sqrt{1 - \rho^2 / R^2}} + \alpha \rho^4$$

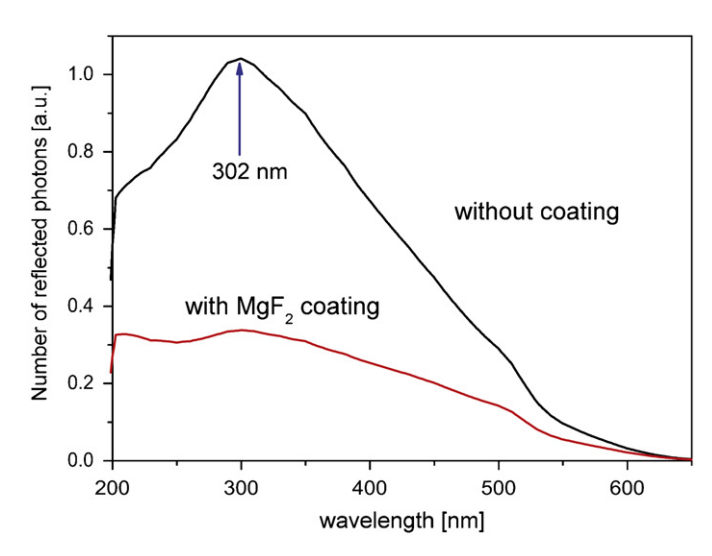


Fig. 18. Spectrum of the photons lost by reflection without and with the MgF₂ coating of the telescope lenses versus the light wavelength.

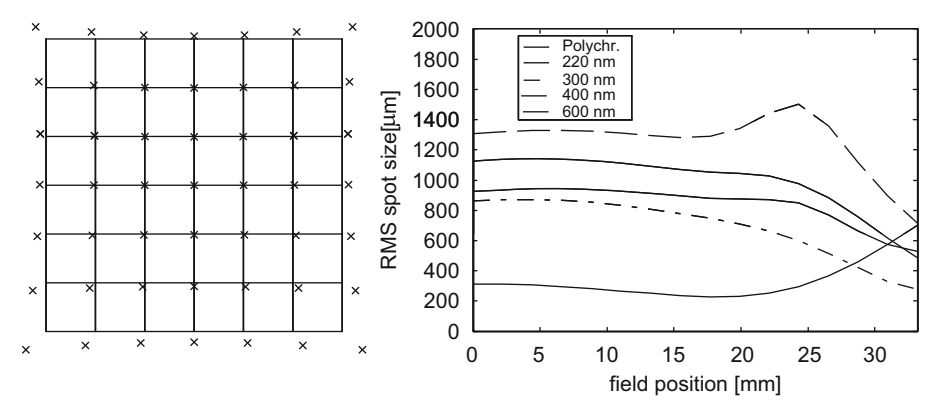


Fig. 17. (a) Image distortion for 300 nm light: the grid intersections represent the ideal case, the crosses are the actual image spot centroids. The crosses span the whole photo-cathode surface. (b) Spot size versus field lens radial position for various light wavelengths.

where z is the coordinate along the lens axis and ρ is the distance from the axis; the parameters defining the surface are the radius of curvature R and the aspherical 4th order coefficient α . The telescope parameters are given in Table 3. Fig. 17 illustrates the achieved image quality.

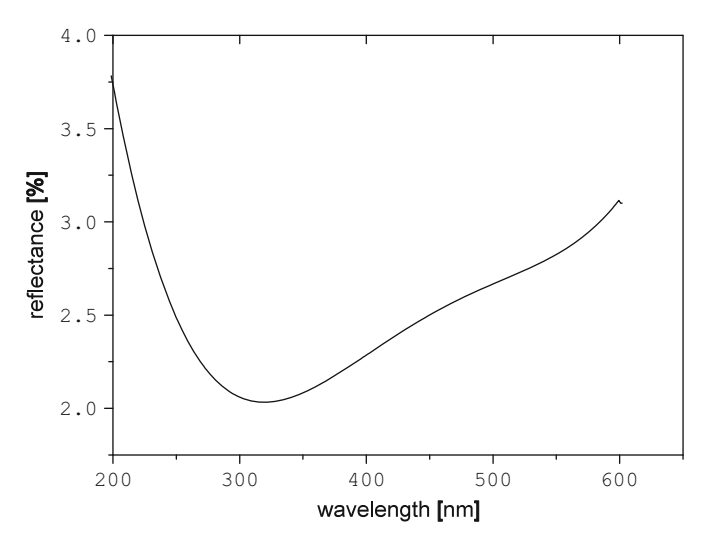


Fig. 19. Measured reflectance of a fused silica surface coated with a single layer of MgF_2 versus light wavelength for normal incidence.

6.3. Lens antireflective coating

The fraction of photons lost by reflection in the telescope has been estimated for the effective Cherenkov photon spectrum: 14.4%. The spectrum of photons lost by reflection is peaked around 300 nm and is shown in Fig. 18.

A single layer MgF_2 coating is effective in most of the wavelength range and its application is a standard procedure. A layer thickness of 75 nm has been chosen in order to minimise the reflection at 300 nm (Fig. 19). It is thus possible to reduce the fraction of photons lost by reflection by about a factor of two, namely to increase the number of detected photons by 8.4% (Fig. 18). Both the telescope lenses are coated with a single layer of MgF_2 optimised for 300 nm photons.

6.4. Tolerances for lens production and mounting

In order to guarantee that the performance of the optical system meets the requirements, the effects of lens imperfections and telescope misalignments cannot exceed given thresholds.

The increase of the spot size and the spot shift have been analysed, assuming reasonable values for the production and alignment tolerances, so to verify the telescope feasibility and to determine the most critical parameters (Tables 4 and 5). The most delicate parameters for lens production are those concerning the correct angle of the planar surface of the field lens, the correct shaping of the aspherical surface of the concentrator and the relative alignment of the centres of the two surfaces of the

Table 4Maximum effect of lens production tolerances.

Parameter	Nominal value	Tolerance (\pm)	Δ Spot-size (μm)	Δ Centroid _Y (μ m)	Δ Centroid _X (μ m)
Surface 1					
Radius	54.94 mm	0.5 mm	3.3	0	0
Surface irregularity		10 fringes	0.08	0	0
Thickness	20.8134 mm	0.1 mm	0.3	1	0
Tilt		0.02°	0.6	2.1	2.1
Decenter		0.1 mm	3.1	11	11
Refractive index		0.001	0.5	1.4	0
Surface 2					
Radius	infinity	50 fringes	0.2	0	0
Surface irregularity		10 fringes	0.08	0	0
Tilt	5°	0.1°	0.2	13.3	13.3
Surface 3					
Radius	20.696 mm	0.06	13	2.8	0
Aspheric coefficient	$-6.13885 \ \times 10^{-5} m^{-3}$	5×10^{-7}	15	2.3	0
Surface irregularity		10 fringes	0.4	0.2	0
Thickness	19.420 mm	0.1 mm	14	0.3	0.3
Tilt		0.02°	0.04	6	6
Decenter		0.05 mm	4	29	29
Refractive index		0.001	14	2.7	2.7
Surface 4					
Radius	– 24.964 mm	0.06 mm	3.3	0	0
Surface irregularity		10 fringes	0.04	0.2	0
Tilt		0.02°	0.5	5.7	5.6
Decenter		0.05 mm	2.7	32	32
Total (in quadrature)			31	48	47

 Δ Spot-size is the change in spot size r.m.s. at 300 nm; Δ centroid $_Y$ is the shift in the spot centroid position projected in the wedge angle plane; Δ centroid $_X$ is the shift in the spot centroid position projected in a plane orthogonal to the wedge angle plane. The total effect does not take into account some parameter correlation and thus it is slightly overestimated.

Table 5Maximum effect of lens mounting tolerances.

Parameter	Nominal value	Tolerance (\pm)	Δ Spot-size (μm)	Δ Centroid _Y (μ m)	Δ Centroid _X (μ m)
Field lens					
Tilt	0	0.05°	0	1.4	1.4
Decenter	0	0.1 mm	0	11	11
Spacing	75.81 mm	0.5 mm	3.3	5.4	0
Concentrator lens					
Tilt	0	0.05°	0	12	12
Decenter	0	0.05 mm	1	61	61
Spacing (to MAPMT)	26.84 mm	0.1 mm	14	1.2	0
Total (in quadrature)			14.4	63	63

 Δ Spot-size is the change in spot size r.m.s. at 300 nm; Δ centroid $_Y$ is the shift in the spot centroid position projected in the wedge angle plane; Δ centroid $_X$ is the shift in the spot centroid position projected in a plane orthogonal to the wedge angle plane. The total effect does not take into account some parameter correlation and thus it is slightly overestimated.

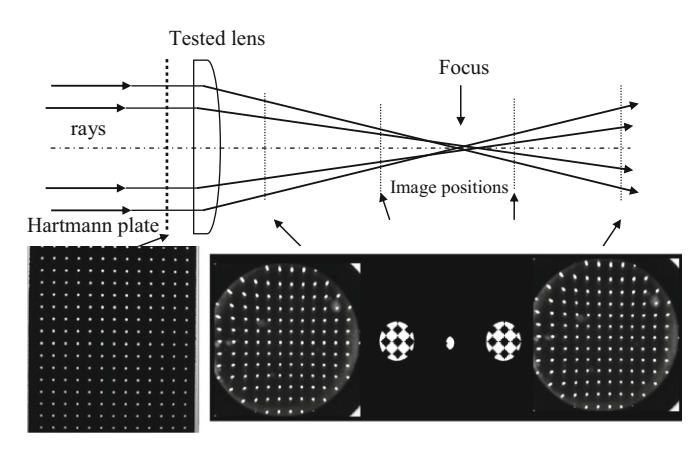


Fig. 20. Sketch illustrating the principle of the Hartmann method.

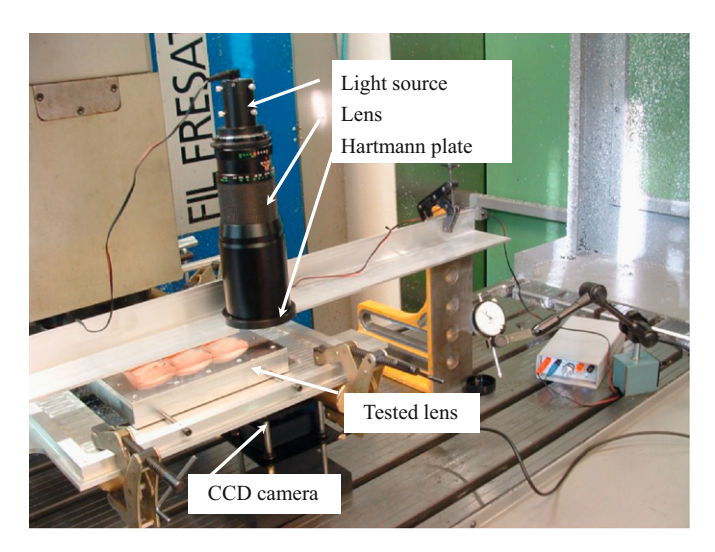


Fig. 21. The setup built for the assessment of the optical quality of the telescope elements and the correct telescope mounting.

concentrator. For the telescope alignment, the most critical parameters are the relative alignment of the two lenses and the distance between the concentrator and the MAPMT.

6.5. A setup for the optical quality assessment

A setup for the optical quality assessment has been designed and built, in order to check the quality of the produced fused silica

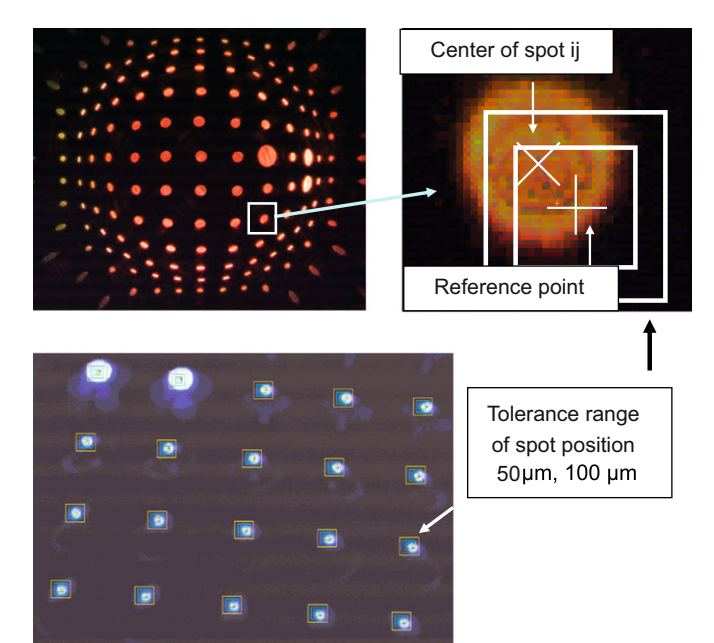


Fig. 22. A typical image collected with the Hartmann setup. The zoom of a spot is shown. The comparison between the spot position in the image and the expected position for the ideal optical object is also shown. The accepted tolerance for the optical object can be translated in an area around the ideal position: if the actual spot is contained in this area, the optical distortions are within tolerances.

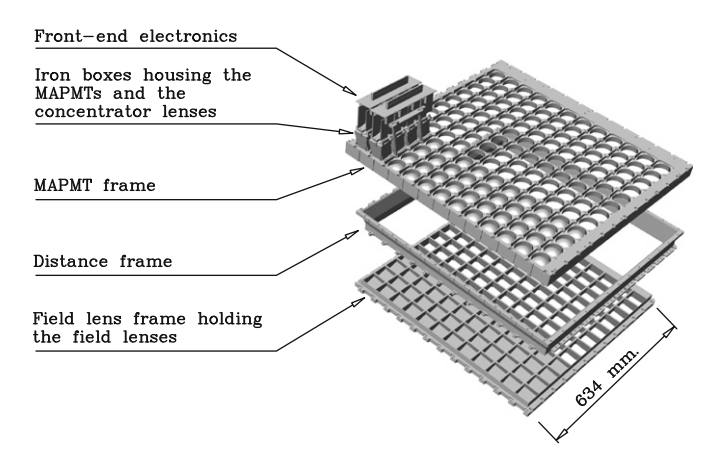


Fig. 23. The three frames that assembled together form the mechanical structures of one of the four quadrants; from bottom to top: the field lens frame, the distance frame and the MAPMT frame.

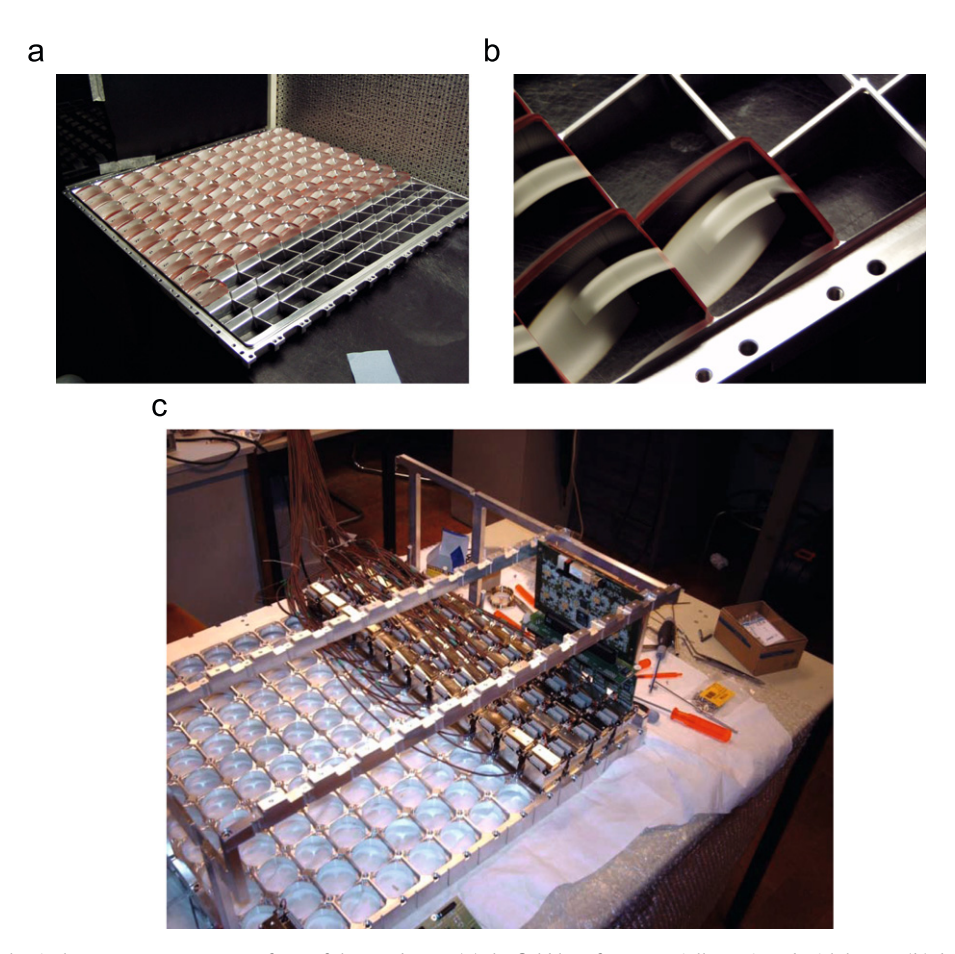


Fig. 24. Pictures of the mechanical structure components of one of the quadrants; (a) the field lens frame partially equipped with lenses; (b) detail of the field lens frame; (c) the MAPMT frame partially equipped with the iron boxes housing the MAPMTs and the concentrator lenses.

lenses at production and the overall quality of the telescopes, after the assembly. The test system is based on the Hartmann method [29] and is suitable for the optical checks of a large number of lenses and telescopes.

The principle of the Hartmann technique (Fig. 20) is based on the use of a mask with a regular array of holes, placed at the pupil of the optical system to be tested. A parallel beam illuminates the optical system through the mask. The image of the spots corresponding to the holes is collected at a defocusing position. The shape of the wavefront can be deduced from the spot image: the aberrations of the optical system can be determined, comparing the reconstructed wavefront with the ideal one. To measure accurately the position of the spots, the defocusing and the separation of the holes have to be quite large to avoid overlapping spot images.

The setup which has been implemented [30] is shown in Fig. 21. The light source is a 462 nm LED, powered with a stabilised power supply, placed in the focus of an expander lens in order to obtain a parallel light beam. The Hartmann plate has 27×27 holes of 0.6 mm diameter and spaced by 1.8 mm. The spot image is collected by a CCD camera: LU130 by Lumenera. A typical image is shown in Fig. 22.

The differences between the actual image and the one calculated assuming nominal design parameters are analysed and provide information about the lens quality.

⁹ Lumenera Corporation, 7 Capella Crt. Ottawa, Ontario, Canada K2E 8A7.

6.6. Lens production

The lens drawings for production have been obtained merging the optical design with those details that allow to assemble the telescopes and their mechanical supports (Section 7). Five-hundred seventy-six field lenses and 576 concentrators are needed for the complete project. The material used is fused silica, type Corning 7980, standard grade F5 by Corning. ¹⁰

The field lenses, having a flat and a spherical surface, require standard optical production; nevertheless, the lens edges exhibit features typical of mechanical components, dictated by the overall mechanical design (Section 7). They have been produced by Gestione Silo.¹¹ About 680 lenses have been produced and their quality has been checked; about 650 satisfy the specification and almost all the pieces not accepted were rejected because of mechanical imperfections at the edges.

The concentrator lenses are formed by a spherical and an aspherical surface: they require a non-standard optical machining. In order to select the producer, lens prototypes have been evaluated using the Hartmann setup (Section 6.5) and, in parallel, with interferometric methods at the Optical Development Workshop of the Czech Academy of Science, Turnov, Czech Republic. The surface roughness was measured at the Optical Workshop of Sincrotrone Trieste, Trieste, Italy. The selected producer is Asphericon. 12 The rejection yield is $\sim 5\%$, mainly due to scratches

¹⁰ Corning Incorporated, One Riverfront Plaza, Corning, NY 14831, USA.

¹¹ Gestione Silo s.r. L., Via Castelpucci 14/D, 50018 Scandicci, Firenze, Italy.

¹² Asphericon GmbH, Wildenbruchstr. 15, 07745 Jena, Germany.

on the lens surface. The total cost of the telescopes is about 20% of the cost of the MAPMTs.

7. Mechanical support and photon detector assembly

The mechanical support of the new photon detection system of the central region of RICH-1 has been designed to satisfy several requirements of the project. It is the support of the MAPMTs and of the optical telescopes; therefore it has to ensure the precise alignment of the optical elements. It is the interface between the new photon detectors and the photon detectors of the peripheral region: it has to ensure the gas tightness necessary for the correct operation of the peripheral photon detectors. It is also the structure to which the support for the components of the MAPMT read-out system is fixed [13].

Each of the four quadrants forming the central detection region of RICH-1 is equipped with an independent mechanical structure. The top-left (top-right) and bottom-right (bottom-left) structures are identical; the design of the top-left and top-right ones are mirror symmetric. Each structure is formed by three different aluminium frames assembled together (Fig. 23): the field lens frame, the spacer frame and the MAPMT frame.

The field lens frame houses the field lenses. This frame is directly interfaced to the atmosphere of the peripheral photon detectors. To guarantee the required gas tightness, the field lenses are glued onto this frame, using a filling glue.¹³ The correct positioning of the field lens in this frame is obtained thanks to machining the field lens, which guarantee a precise mechanical reference on the lenses themselves (Fig. 24) and by a specific design of the individual lens holders: the correct lens location is reached when two lens edges are in contact with two sides of the holder. The residual position uncertainty depends on the lens and frame machining precision: both are better than 0.1 mm. The correct positioning (location and inclination) of the field lenses is checked using the quality assessment setup based on the Hartmann principle. The frame with the lenses is mounted on the support of a milling machine with micrometric position resolution. The Hartmann setup is aligned with respect to the reference marks of the field lens frame. The frame is then moved so to check the location and angular alignment of each single lens. The dead area between the field lenses is about 2% of the surface

The spacer frame establishes the correct distance between the field lens and the concentrator. The volume enclosed among the field lens frame, the MAPMT frame and the spacer frame is flushed with nitrogen to keep it dry and clean.

The MAPMT frame (Fig. 24) houses the soft iron boxes (Section 4.1 and Fig. 7), each of them including a concentrator lens, a MAPMT and the voltage divider used to supply the MAPMT. The four elements forming these boxes are nickel coated to protect them against rusting. They are screwed together and the magnetic shielding obtained is satisfactory (Section 4.1 and Fig. 8). The MAPMTs, already coupled to the voltage divider PCBs, are inserted in the main body of the boxes. A small soft iron plate, covering part of the PCB and screwed onto the main body, completes the magnetic closure of the box at the rear side. The concentrator lens support is mounted onto the front side of the main body. The lens seat is circular and the lens is centred and kept in place blocking it by a dedicated ring screwed onto the lens support. This design has been validated checking the lens alignment with respect to the lens support and the alignment reproducibility by the Hartmann

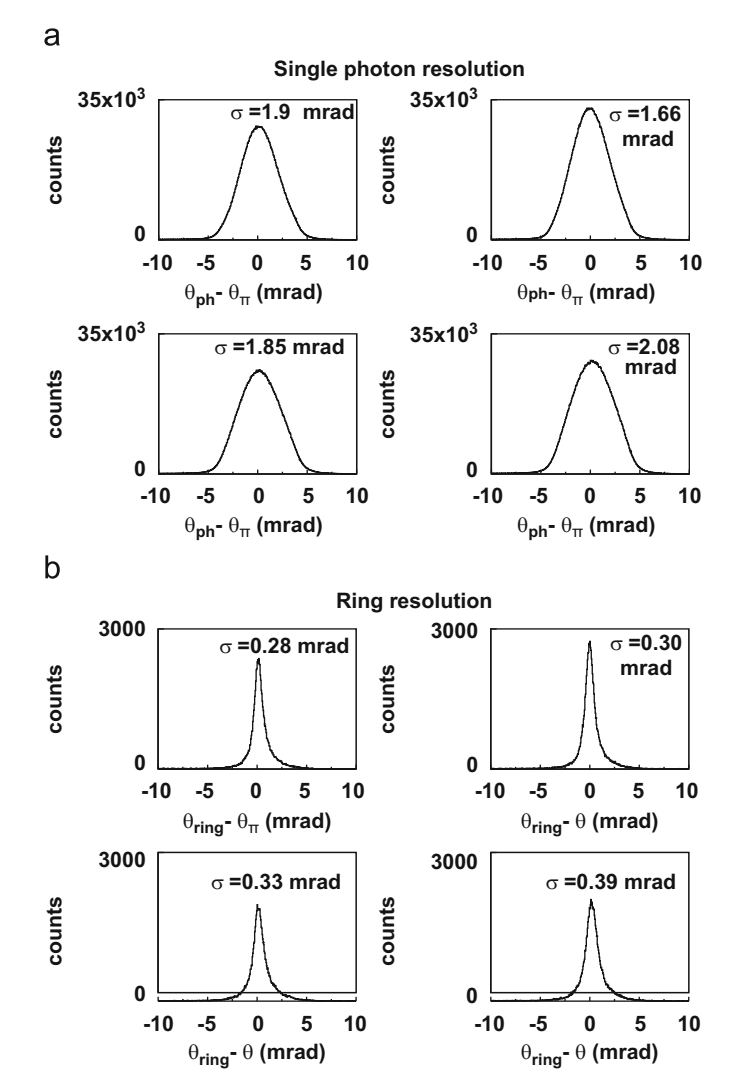


Fig. 25. Resolution on the Cherenkov angle for the four MAPMT photon detector panels; (a) using single photon information; (b) from the whole ring image.

setup. The residual misalignment is below the sensitivity of the measurement.

To perform the quality control of the whole telescopes, each complete structure is first assembled without introducing the MAPMTs in the iron boxes. It is then possible to use the Hartmann setup, because the image can be collected downstream of the telescope. The method used is the same as employed for the quality control of the alignment of the lenses glued to the field lens frame, namely the Hartmann setup is fixed, while the complete panel is moved on a milling machine. The telescope imperfections are due to deficiencies of the concentrator lens holders. They are made, as the whole MAPMT box, by soft iron. This material, required to form a magnetic screen around the MAPMT, is not ideal for precise machining. When small telescope imperfections are detected, it is possible to correct for them. The corrections are obtained by tilting the concentrator lens with respect to the MAPMT frame, to which the complete soft iron box is screwed: the optical properties of the telescope can be almost completely recovered. After applying these corrections, 70% of the telescope exhibit a deviation of the images collected by the Hartmann setup with respect to the design image, corresponding to a shift of the image in the photocathode plane, below $50 \,\mu m$, 20% between 50 and 100 μm and 10% between 100 and 150 μm .

¹³ The lens and frame surfaces to be glued are treated with the primer Rhodosil 131; the glue is CAF1. Primer and glue are produced by Bluestar Silicones, 19 avenue Georges Pompidou Cedex 03, Lyon 69486, France.

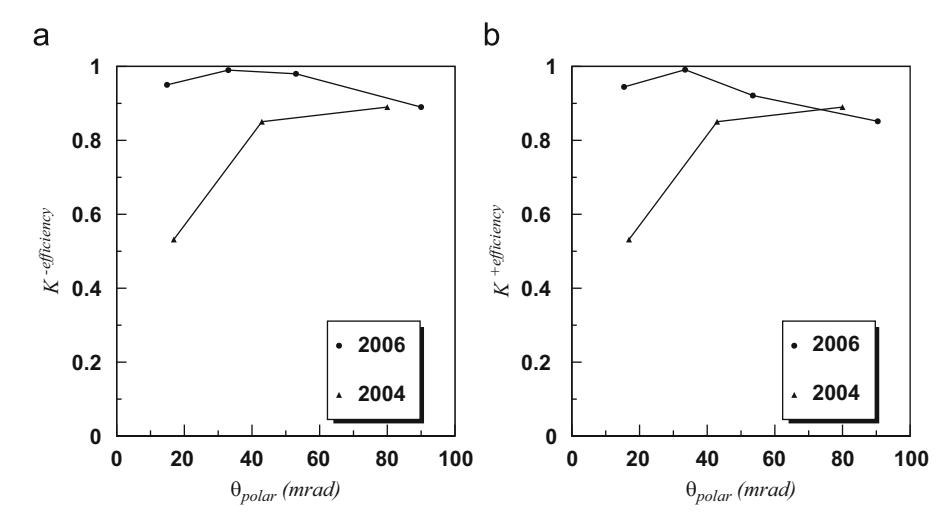


Fig. 26. PID efficiency versus polar angle for a sample of Ks from Φ- decay; Φ- decay events are selected using the kinematic reconstruction; (a) K⁻; (b) K⁺.

8. Photon detector performance

The upgraded RICH-1 detector, including the new MAPMT detector part, was successfully commissioned at the beginning of the COMPASS 2006 data taking [20,31].

The overall measured time resolution has 1 ns r.m.s., mainly due to the different geometrical path length of the Cherenkov photons [13].

The average number of detected photons per ring is about 56 for saturated rings. The resolution on the measured Cherenkov angle using single photon information is $\sim\!2\,\mathrm{mrad}$ (Fig. 25). The resolution of the measured Cherenkov angle from the whole ring image is $\sim\!0.3\,\mathrm{mrad}$: σ_{ph} and σ_{ring} scale almost exactly according to the square root of the number of photons, confirming the negligible effect of the residual background.

No efficiency reduction is observed for particle scattered at small scattering angles, whose images are formed in a photon detection area where the photon flux is extremely high: up to 1 MHz per channel [13]. This is shown in Fig. 26, where the efficiency obtained with the upgraded counter is compared with the previous efficiency figures.

9. Conclusions

The fast photon detection system for the upgrade of COMPASS RICH-1 required a careful design and a challenging construction. It was built and commissioned in about 18 months and it fulfils its design goals and the requirements of the COMPASS experiment.

Cherenkov imaging counters are nowadays extensively used in many sectors of particle and nuclear physics. Concerning the future programmes, emphasis is put on requirements such as increased angular resolution, fast response, rate capability and increased time resolution [32]. The new photon detection system of the central region of COMPASS RICH-1, with a system characterised by high detected photon yield, fast response and high rate capability, designed to match the specific requirements of the COMPASS experiment, is a relevant step towards the next generation of Cherenkov imaging counters.

Acknowledgements

The authors are grateful to the colleagues of the COMPASS Collaboration for constant support and help. This work was

supported in part by the BMBF (Germany), by MEYS (Czech Republic), Grant 1P04LA211, and the European Community-research Infrastructure Activity under the FP6 Programme (Hadron Physics, RII3-CT-2004-506078).

References

- The COMPASS Collaboration, Proposal, CERN/SPSLC/96-14, SPSC/P297, March 1, 1996, Addendum, CERN/SPSLC/96-30, SPSLC/P297, Addendum 1, May 20, 1996
- [2] E.S. Ageev, et al.COMPASS Collaboration, Phys. Lett. B 612 (2005) 154; V.Yu. Alexakhin, et al.COMPASS Collaboration, Phys. Rev. Lett. 94 (2005) 202002.

E.S. Ageev, et al.COMPASS Collaboration, Eur. Phys. J. C41 (2005) 469;

E.S. Ageev, et al.COMPASS Collaboration, Phys. Lett. B 633 (2006) 25; V.Yu. Alexakhin, COMPASS Collaboration, Phys. Lett. B 647 (2007) 8;

E.S. Ageev, et al. COMPASS Collaboration, Nucl. Phys. B 765 (2007) 31;

V.Yu. Alexakhin, COMPASS Collaboration, Phys. Lett. B 647 (2007) 330;

M. Alekseev, et al.COMPASS Collaboration, Eur. Phys. J. C52 (2007) 255;

M. Alekseev, et al.COMPASS Collaboration, Phys. Lett. B 660 (2008) 458;

M. Alekseev, et al.COMPASS Collaboration, Phys. Lett. B 673 (2009) 127;

M. Alekseev, et al.COMPASS Collaboration, Phys. Lett. B 676 (2009) 31;

M. Alekseev, et al.COMPASS Collaboration, Phys. Lett. B 680 (2009) 217;

M. Alekseev, et al., COMPASS Collaboration, Eur. Phys. J. C64 (2009) 171; M. Alekseev, et al., COMPASS Collaboration, Observation of a JPC = I^{-+} exotic resonance in diffractive dissociation of 190 GeV/c π^- into $\pi^-\pi^-\pi^+$, Phys. Rev.

- [3] P. Abbon, et al.COMPASS Collaboration, Nucl. Instr. and Meth. A 577 (2007) 455.
- [4] E. Albrecht, et al., Nucl. Instr. and Meth. A 502 (2003) 112;
 E. Albrecht, et al., Nucl. Instr. and Meth. A 518 (2004) 586;
 E. Albrecht, et al., Nucl. Instr. and Meth. A 553 (2005) 215.

Lett., submitted for publication

- [5] RD26 Collaboration, status reports: CERN/-DRDC 93-36, 94-49, 96-20; The ALICE Collaboration, Technical Design Report of the High Momentum Particle Identification Detector, CERN/ LHCC 98-19, ALICE TDR 1, 14 August 1998; F. Piuz, Nucl. Instr. and Meth. A 502 (2003) 76.
- [6] P. Abbon, et al., Nucl. Instr. and Meth. A 589 (2008) 362.
- [7] M.J. French, et al., Nucl. Instr. and Meth. A 466 (2001) 359.
- [8] E. Albrecht, et al., Nucl. Instr. and Meth. A 502 (2003) 266. [9] E. Albrecht, et al., Nucl. Instr. and Meth. A 502 (2003) 236.
- [10] F. Sozzi, Diploma Thesis, University of Trieste, Italy, 2003.
- [11] C. Santiard, et al., Gassiplex: a low noise analog signal processor for readout of gaseous-detectors, Presented at the Sixth Pisa Meeting on Advanced Detector, La Biodola, Isola d'Elba, Italy, May 1994.
- [12] M. Alekseev, et al., Nucl. Instr. and Meth. A 553 (2005) 53;
 - P. Abbon, et al., Nucl. Instr. and Meth. A 567 (2006) 114;
 - P. Abbon, et al., Nucl. Instr. and Meth. A 572 (2007) 419;
 - P. Abbon et al., Studies for a fast RICH, World Scientific ISBN 981-256-798-4, Singapore, 2006, p. 103;
 - P. Abbon, et al., Nucl. Instr. and Meth. A 580 (2007) 906;
 - P. Abbon, et al., Nucl. Phys. B, Proc. Suppl. 172 (2007) 75;
 - P. Abbon, et al., Czech. J. Phys. 56 (2006) 318;
 - P. Abbon, et al., Czech. J. Phys. 56 (2006) 327;
 - P. Abbon, et al., Czech. J. Phys. 56 (2006) 333;
 - P. Abbon, et al., Nucl. Instr. and Meth. A 581 (2007) 419.
- [13] P. Abbon, et al., Nucl. Instr. and Meth. A 587 (2008) 371.

- [14] I. Ariño, et al., Nucl. Instr. and Meth. A 516 (2004) 445.
- [15] D.R. Broemmelsiek, Nucl. Instr. and Meth. A 433 (1999) 136.
- [16] The LHCb Collaboration, LHCb Technical Design Report, CERN/LHCC/2000-37; E. Albrecht, et al., Nucl. Instr. and Meth. A 488 (2002) 110.
- [17] E. Albrecht, et al., Nucl. Instr. and Meth. A 456 (2001) 190 (Private communication by E. Fokitis).
- [18] HAMAMATSU, Multianode Photomultiplier tube assembly H8711, Technical Data.
- [19] I. Chirikov-Zorin, et al., Nucl. Instr. and Meth. A 456 (2001) 310;
 I. Chirikov-Zorin, et al., Nucl. Instr. and Meth. A 461 (2001) 587.
- [20] G. Pesaro, Diploma Thesis, University of Trieste, Italy, May 2007.
- [21] E. Rocco, Diploma Thesis, University of Trieste, Italy, December 2005.
- [22] P. Abbon, et al., Nucl. Instr. and Meth. A 595 (2008) 177.
- [23] F. Gonnela, M. Pegoraro, CERN-LHCC-2001-034, p. 204-8.
- [24] H. Fischer, et al., Nucl. Instr. and Meth. A 461 (2001) 507.
- [25] G. Ingelman, et al., Comput. Phys. Commun. 101 (1997) 135.

- [26] GEANT-detector description and simulation tool, CERN Program Library Long Writeup W5013, http://www.asdoc.web.cern.ch/www.asdoc/geant_html3/geantall.html>.
- [27] G. Ingelman, et al., Comput. Phys. Commun. 101 (1997) 108.
- [28] D. Kramer, Diploma Thesis, Technical University of Liberec, Czech Republic, June 2005.
- [29] J. Hartmann, Zt. Instrum. 20 (1900) 47; I. Ghozeil, Hartmann and other screen tests, in: D. Malacara, Optical Shop Testing, second ed., John Wiley & Sons Inc., New York, ISBN 0-471-52232-5, 1992 (Chapter 10).
- [30] J. Polak, Diploma Thesis, Technical University of Liberec, Czech Republic, October 2007.
- [31] P. Abbon, et al., Nucl. Instr. and Meth. A 595 (2008) 233.
- [32] Proceedings of the Sixth International Workshop on Ring Imaging Cherenkov Counters (RICH2007), Trieste, Italy, 15–20 October 2007, Nucl. Instr. and Meth. A 595 (2008).